Fermilab Library
0 1160 0052446 6

SSC-SDC-30

SSC-SDC
SOLENOIDAL DETECTOR NOTES

RECONSTRUCTION OF TOP QUARKS IN AN SSC SOLENOIDAL DETECTOR

R.J. Hollebeek, P.K. Sinervo, H.H. Williams

May 9, 1990

Reconstruction of Top Quarks in an SSC Solenoidal Detector

R. J. Hollebeek, P. K. Sinervo and H. H. Williams

University of Pennsylvania Penn U.
Philadelphia, PA 19104

May 9, 1990

Abstract

A study of the detection of top quark events with M_{top}= 150 GeV/c^2 in an SSC solenoidal detector is described. The electron + jets final states resulting from $t\bar{t}$ production were generated using ISAJET 6.22 and the resulting detector response was modelled with the QFL detector simulation. Issues such as lepton isolation, detector energy resolution, and the effect of multiple interactions are discussed. A crude technique to fully reconstruct a small fraction of the $t\bar{t}$ events is described, and the expected signal from such a search is presented.

1 Introduction

In previous SSC workshops and conferences, a substantial amount of work has centered on the search for new particles on the mass scale of several hundred GeV/c^2 (see, for example, [1]–[4]), but relatively little has been reported on attempts to reconstruct particles that have mass scales of order 100 GeV/c^2 and have complicated decay modes. The top quark is now one such particle as the recent published CDF results exclude at 95% confidence level a standard model top quark with a mass < 77 GeV/c^2 [5] (the latest preliminary results exclude a mass < 89 GeV/c^2 [6]), and the current ensemble of Electroweak data prefer a top quark with mass $\lesssim 200$ GeV/c^2 [7].

Although we expect the top quark to be discovered at the Fermilab Tevatron in the next five years if its mass is $\lesssim 200$ GeV/c^2, we also believe that a top quark with mass between 100 and 200 GeV/c^2 has a significant impact on the physics one does at the SSC and on the design of the detector one should construct to perform this physics. For example, $t\bar{t}$ production at the SSC has a cross section of 12 nb for a top quark mass of 150 GeV/c^2, or a rate of 12 Hz at SSC design luminosities. The decay of these two quarks will yield a pair of W bosons, which decay either hadronically or leptonically, and a pair of b quark jets. This results in a rate of W boson pair production that could swamp the rate of W pairs from the decay of a Higgs particle. The argument continues that because of this, most exotic physics signatures requiring the presence of a pair of W bosons in the final state are now beyond our reach at the SSC.

We therefore argue that the detection and study of the top quark should be a high priority for an SSC experiment using a general-purpose detector. Given the copious rate of $t\bar{t}$ events, it will almost surely be one of the calibration physics process for an SSC detector, in the same way that b quark physics is being used as a means of calibrating the abilities of the CDF detector. Perhaps more important is the fact that to actually see what one believes is new physics at the SSC, it first will be necessary to understand all of the old and expected physics. In this sense, the ability to detect and reconstruct top quarks will play an important part in establishing the credibility of an SSC detector.

With this motivation, we have been studying the final states produced in $t\bar{t}$ decays, focusing on those channels that produce an isolated electron, an energetic neutrino and several jets. We have chosen a top quark mass of 150 GeV/c^2 in our study as this value lies midway between the direct lower limit and the theoretical higher mass limit. We have used the ISAJET 6.22 event generator to calculate the $t\bar{t}$ production and decay, and have simulated the response of a solenoidal 4π detector using the QFL simulation program. We have considered in turn:

- the isolation properties of the energetic lepton;
- measurement of missing transverse energy;
- the effect of calorimeter tower thresholds on jet cluster reconstruction;
- the effect of multiple interactions on lepton isolation, and jet cluster resolution;
- the ability to reconstruct the $W \to q\bar{q}$ decays using calorimeter clusters; and
- the use of b quark tagging to fully reconstruct $t\bar{t}$ events.

2 Event Generation and Detector Simulation

We used the ISAJET 6.22 Monte Carlo program[8] to generate direct $t\bar{t}$ production and decay using the standard decay table (the top quark branching fractions are 1/3 into $u\bar{d}b$ and $c\bar{s}b$ and 1/9 into each of the semi-leptonic channels). We then passed the events through the QFL detector simulation[9], which models an idealized SSC detector that consists of a solenoidal tracking volume followed by a spherical calorimeter divided into an electromagnetic and hadronic compartment. The solenoidal magnetic field strength was set to 15 kiloGauss, and the radius and length of the tracking volume was set to 1.7 m and 3.4 m respectively.

The calorimeter response in QFL is modelled by parametrizing the longitudinal and lateral shower shapes [10], summing up the energies observed in the electromagnetic (EM) and hadronic (HAD) compartment, and then smearing these energies using a Gaussian lineshape. In our studies, the standard resolutions of the electromagnetic and hadronic calorimeters were

$$\frac{\sigma_{em}}{E_{em}} = \frac{0.15}{\sqrt{E_{em}}} + 0.01 \tag{1}$$

$$\frac{\sigma_{had}}{E_{had}} = \frac{0.50}{\sqrt{E_{had}}} + 0.03. \tag{2}$$

We defined the thickness of the EM calorimeter to be 25 radiation lengths and the hadronic calorimeter's thickness to be 10 absorption lengths. The calorimeter covered ± 5.0 units of rapidity and was uniformly segmented in $\eta - \phi$ space into a 200×100 grid, giving tower sizes $\Delta\eta \times \Delta\phi = 0.05 \times 0.063$.

Although QFL is a simple simulation that does not attempt to include detector boundaries, cracks or a more realistic geometry, it has the virtue of providing us with a "best-case" simulation that is very rapid. It does include shower spreading and the effect of "sweeping"

of low-energy charged particles due to the magnetic field, both of which are considered important effects.

Since we were interested in studying the $t\bar{t}$ final states where an energetic electron is present, we generated all $t\bar{t}$ decay modes but only retained and simulated those events in which we found a generated electron with $P_T > 10$ GeV/c. Although most such events result from one of the top quarks decaying semileptonically, this selection did include those final states where the electron resulted from a semileptonic decay of a b or c quark. For the bulk of this study we used a sample resulting from the generation of 80 000 ISAJET events. Approximately 1/3 of these events had at least one electron with $P_T > 10$ GeV/c, providing a simulated data sample of ~27 000 events. The sensitivity of the sample is about 6 pb^{-1}.

3 Event Reconstruction

We first reconstructed the simulated events using the calorimeter information created by QFL, which consists of the amount of EM and HAD energy in each tower, and the generated lepton information.

3.1 Electron Reconstruction

We "reconstructed" electrons by extrapolating each generated electron with $P_T > 10$ GeV/c to the calorimeter tower it intersects, and then defining an EM cluster to be the set of towers within ± 2 towers in η and ± 1 tower in ϕ that have at least 0.1 GeV of EM transverse energy. This algorithm does not generate "fake" EM clusters created by the overlap of charged tracks with π^o's or γ's, or candidates resulting from a $\pi^{\pm}$ showering in the EM calorimeter, but we make the assumption that the electron ID (whatever it is) is sufficently powerful to reject such fakes. However, electrons resulting from Dalitz decays are generated by ISAJET, and so they would be reconstructed as EM candidates by this algorithm. The EM transverse energy sum of the towers in the cluster, E_T^{em}, is defined as the transverse energy of the electron candidate. The hadronic transverse energy sum of the towers in the cluster is used to calculate the ratio of hadronic-to-electromagnetic energy, h/em, which we use as a measure of the isolation of the electron candidate. Since we are not simulating the tracking capabilities of the detector, we simply associated the generated electron P_T with the observed P_T of the candidate.

We also defined two other measures of lepton isolation: The first is the transverse energy in the towers that are ± 3 units in η and ± 2 units in ϕ from the center of the electromagnetic cluster, E_T^{iso} (the sum excludes the towers in the EM cluster). This is effectively the energy in the calorimeter bordering the cluster and includes $\sim$ 30 towers. The second is the

transverse energy of the towers in a cone of radius $R \equiv \sqrt{\Delta\eta^2 + \Delta\phi^2}$ of 0.4 units, $E_T^{0.4}$. This includes approximately four times more towers than does the "border tower" E_T, E_T^{iso}.

3.2 Jet Candidates

We defined jet clusters using the nearest-neighbour clustering algorithm, CLUSTR, a standard QFL utility. This clustering algorithm considers all towers with total E_T above a seed tower threshold, and combines all neighbouring towers above a shoulder tower threshold with the seed tower into a cluster. The clustering does not include an adjacent tower if the ratio of the adjacent tower's E_T to the E_T of the tower in the cluster is too large. Finally, all resulting clusters that are within a cone of 0.7 are merged together into a single cluster.

The parameter values we used in this study are shown in Table 1. The energy thresholds are substantially lower than those used in earlier SSC studies [9], primarily because we are interested in jets with rather low transverse energies ($\sim$ 15 GeV). In order to improve the energy resolution of the jet clusters, after the clusters had been reconstructed we redefined the energy of the jet clusters by summing up all the EM and HAD towers above an E_T threshold of 0.050 GeV in a cone of radius $R = 0.5$ centered on the energy-weighted centroid of the jet cluster. This procedure in effect adds into the cluster those towers that had not been included in the cluster because they were not in proximity to a valid seed tower.

We calculated the 4-momentum of a jet by considering each tower in the cluster to represent a massless particle with an energy equal to the observed energy in the tower and then summing the 4-momenta of these "particles" together to form the 4-momentum we associate with the jet cluster.

3.3 Muon Candidates

We defined μ candidates using the generated μ information. All generated μ's with $P_T >$ 10 GeV/c were extrapolated to the calorimeter, and the same isolation variables were calculated for each candidate as in the case of the electrons.

3.4 Missing E_T

We defined the missing energy vector to be the vector opposite the sum of the vectors defined by the direction of each tower from the interaction vertex multipled by the total energy observed in that tower. The $\not{E}_T$ vector was the projection of the missing energy vector onto the $r - \phi$ plane.

4 Event Selection and Analysis

We interpret the $\not\!\!E_T$ vector as the transverse energy vector of the undetected neutrino, and define the transverse mass as

$$M_T^{e\nu} \equiv \sqrt{2E_T^{em}\,\not\!\!E_T(1-\cos\phi^{e\nu})}, \tag{3}$$

where $\cos\phi^{e\nu}$ is the opening angle between the electron and the neutrino in the $r-\phi$ plane. We show in Fig. 1 the generated $M_T^{e\nu}$ distribution for the $t\bar{t}$ events, as well as the measured E_T distribution for the electron and neutrino. The $M_T^{e\nu}$ distribution shows the characteristic Jacobian lineshape from the decay of a real W boson. The falling E_T spectra of the W daughters reflects the fact that the W boson is produced with a significant amount of P_T and P_L.

4.1 Electron Selection

We show in Fig. 2 the distribution of the three isolation variables, h/em, $E_T^{iso}$and $E_T^{0.4}$, for all of the electron candidates in the sample. One can see that the electrons are locally well isolated, with almost all candidates having $E_T^{iso}<$ 2.0 GeV. The amount of energy deposited in the cone of $R = 0.4$ is about four times what one observes in the border towers, which is roughly consistent with what one expects on the basis of the number of towers included in the two different sums.

To select a sample of isolated electrons, we require the electron candidates to have:

- $|\eta| < 3.0$
- $E_T>$ 20 GeV
- $h/em<$ 0.10
- $E_T^{iso}<$ 5.0 GeV
- $E_T/P_T<$ 1.5

A summary of the number of events passing each cut is given in Table 2. The number of events with at least one electron satisfying these requirements was 13 746. There were $\sim$ 660 events having two electrons, and 4 events with 3 electron candidates. We found that only 3% of the candidates surviving the electron selection came from semileptonic b quark decays.

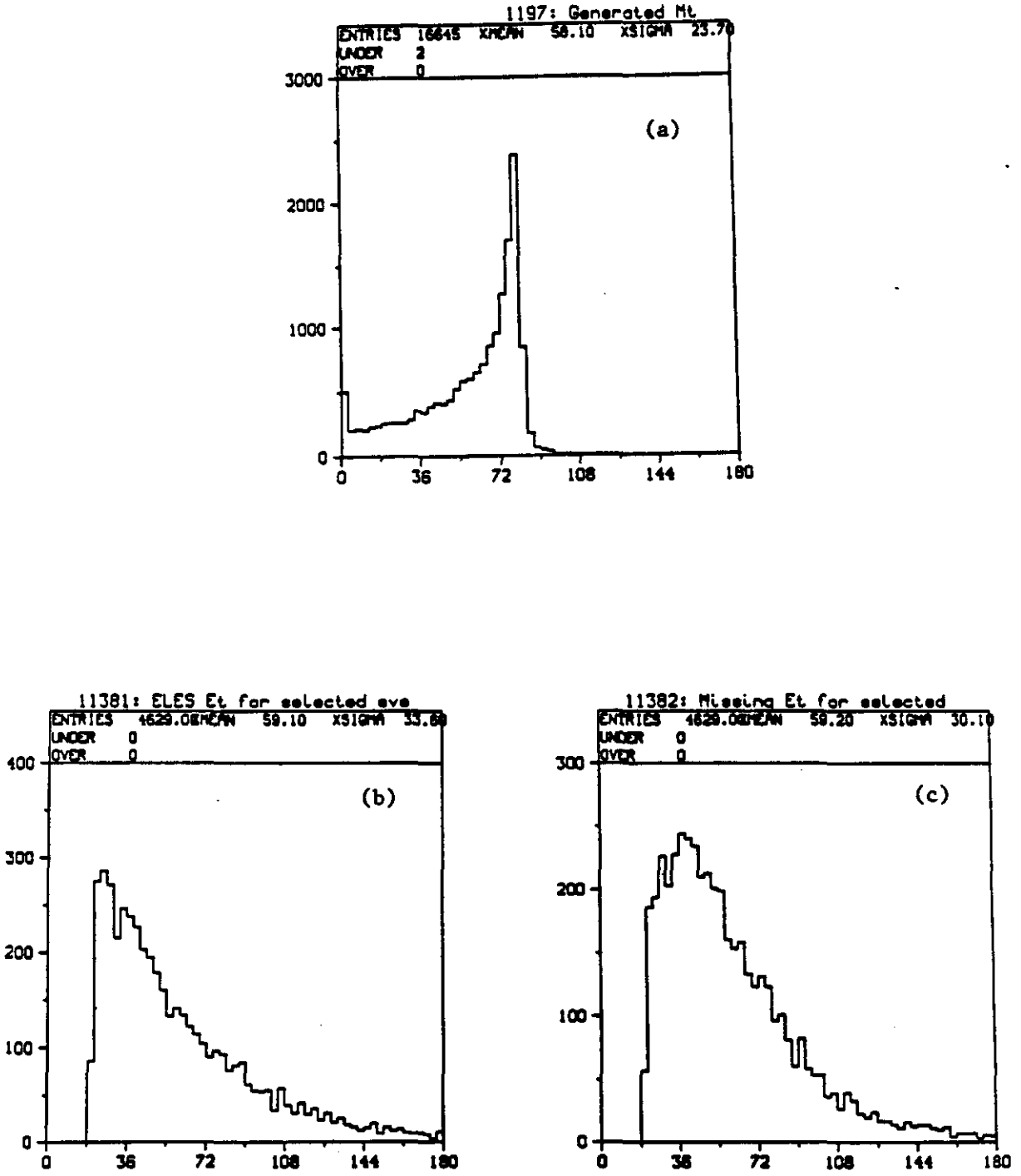

Figure 1: The generated transverse mass distribution for the $t\bar{t}$ events with at least one electron with $P_T > 10$ GeV is shown in (a). The measured E_T and $\not{E}_T$ in these events is plotted in (b) and (c), respectively.

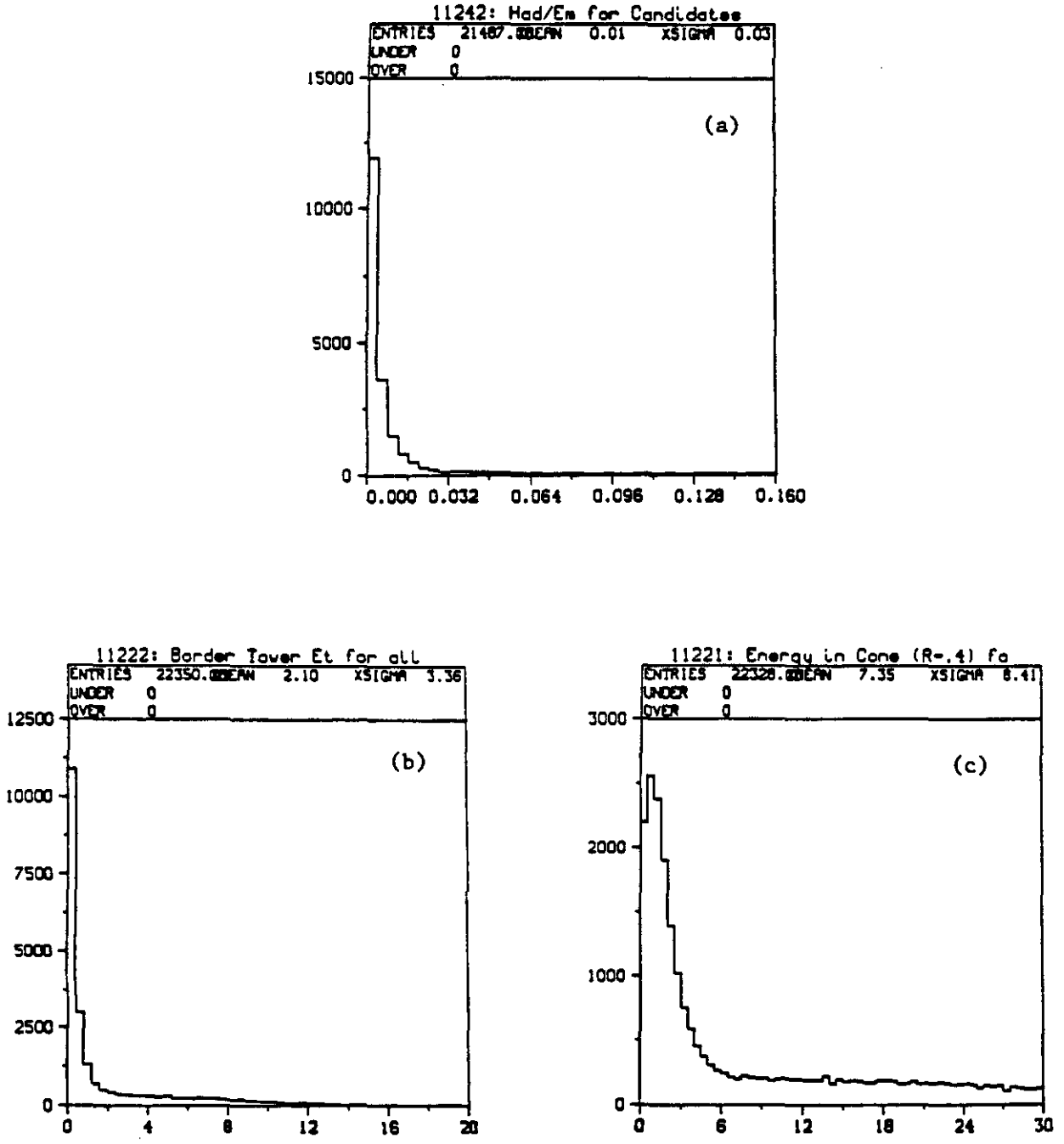

Figure 2: The h/em, E_T^{iso} and $E_T^{0.4}$ distributions for all electron candidates with $E_T > 20$ GeV and $|\eta| < 3$.

4.2 $\not{E}_T$ Resolution

We required $\not{E}_T >$ 20 GeV in order to select events with an energetic neutrino. The observed transverse mass distribution is shown in Fig. 3(a), and can be compared with the generated transverse mass distribution in Fig. 1. The histogram of the difference between the measured and generated $M_T^{e\nu}$ is shown in Fig. 3(b). The smearing in the $M_T^{e\nu}$ variable results primarily from the $\not{E}_T$ resolution, which itself results from several effects:

- the presence of additional neutrinos in the event arising from the decay of the other W in the event and from semileptonic decays of b and c quarks;
- the presence of energetic muons;
- the calorimeter energy resolution; and
- the finite η coverage of the detector.

4.2.1 Additional Neutrinos

We investigated the effect additional ν's had on the $\not{E}_T$ resolution by summing the momentum vectors of all the ν's in an event together and then plotting the magnitude of the projection of this vector along the direction of the primary ν_e resulting from the decay of the W boson. This distribution is shown in Fig. 4(a) and consists of two components. One is essentially a δ-function centered at zero and contains approximately half the events. The other component is much broader and is skewed toward negative values. The latter is due to those events where either the other W in the event has decayed leptonically (about 30% of all events) or one of the b quarks has decayed semi-leptonically. The net effect is almost large enough to account for the observed smearing in $M_T^{e\nu}$.

4.2.2 Calorimeter Resolution

To determine the effect played by calorimeter resolution in the $M_T^{e\nu}$ measurement, we reran the simulation with the resolution of the calorimeters set to

$$\frac{\sigma_{em}}{E_{em}} = \frac{0.20}{\sqrt{E_{em}}} + 0.01 \tag{4}$$

$$\frac{\sigma_{had}}{E_{had}} = \frac{0.75}{\sqrt{E_{had}}} + 0.03. \tag{5}$$

The resulting $M_T^{e\nu}$ distribution is shown in Fig. 4(b) and the distribution of the measured minus the generated $M_T^{e\nu}$ is shown in Fig. 4(c). These are very similar to the distributions shown in Fig. 3, thereby illustrating that calorimeter energy resolution does not appear to be the primary source of $\not{E}_T$ smearing in these events.

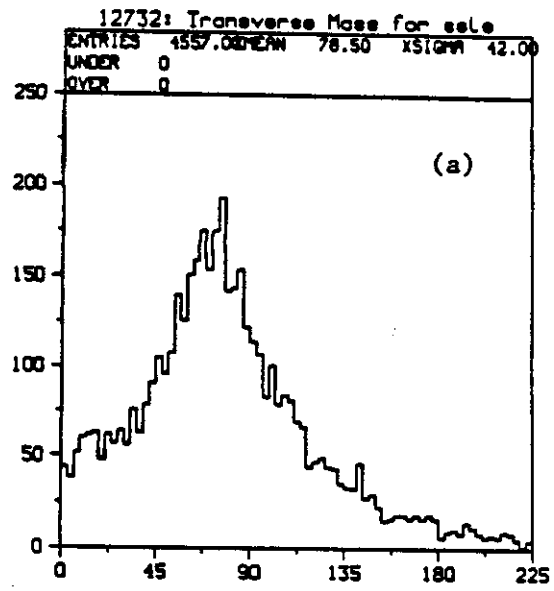

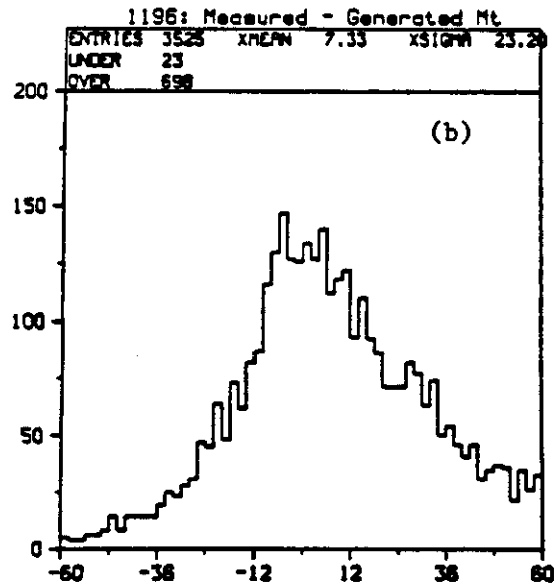

Figure 3: The observed $M_T^{e\nu}$ distribution is shown in (a) for the events passing the electron and $\not{E}_T$ selection. The difference between the measured and generated $M_T^{e\nu}$ is histogrammed in (b).

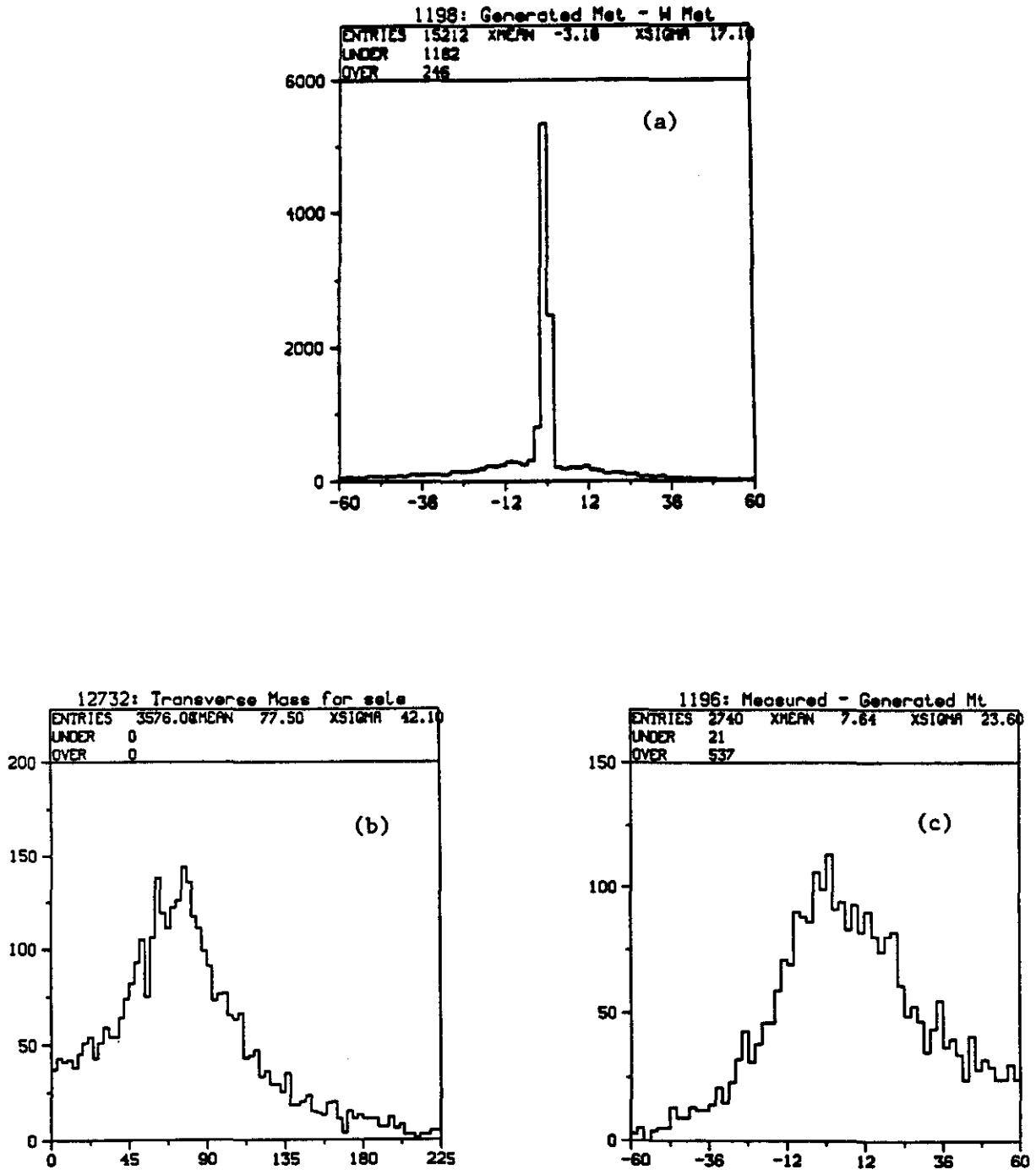

Figure 4: The component of the vector sum of all ν's in the event (excluding the primary ν_e from the W decay) along the direction of the primary ν_e is shown in (a). The $M_T^{e\nu}$ distribution and the difference between the measured and generated $M_T^{e\nu}$ for a calorimeter with poorer energy resolution is shown in (b) and (c), respectively.

4.2.3 Effect of a Finite Beam Hole

We also considered the effect of particles escaping the detector through the beam holes at $|\eta| > 5.0$ by summing the momenta of all generated particles with $|\eta| > 5.0$ and histogramming the magnitude of the resultant vector projected onto the $r - \phi$ plane. The result is shown in Fig. 5(a). The measured $\not{E}_T$ smearing resulting from this affect is about a factor of two smaller than that resulting from additional ν's in the event, and is roughly comparable to the contribution from the calorimeter resolution.

To understand how sensitive the $\not{E}_T$ resolution is to the size of the beam hole, we also calculated the vector sum of the momenta of all particles with $|\eta| > 5.5$ and with $|\eta| > 6.0$. We show the distributions of the size of the transverse component of these vector sums in Fig. 5(b) and (c). We see that the width of this distribution is a relatively weak function of the maximum η coverage for these η values.

We do not know the reliability of the Monte Carlo prediction for the $\not{E}_T$ at large η, but our results indicate that one does not rapidly improve the $\not{E}_T$ resolution by modest increases in η coverage. However, since the contribution of the finite beam hole to the $\not{E}_T$ resolution is small compared to the effect of real $\not{E}_T$ generated by other neutrinos, we would conclude that any real gain in $\not{E}_T$ resolution in $t\bar{t}$ events would be small.

4.3 Jet Resolution

We considered only those jet clusters in the event that satisfied:

- $|\eta| < 3.0$, and
- $E_T > 15$ GeV.

This selection is relatively efficient for jets from the partons arising from the decay of the $t\bar{t}$ system, as illustrated in Fig. 6 were we compare the η and E_T distributions for the $t\bar{t}$ jets and the jets resulting from other partons in the event.

In order to understand the properties of the jets in the events satisfying the electron and neutrino requirements, we identified each jet with the parton in the event that best matched the jet in $\theta - \phi$ space. We estimate that this procedure correctly associated over 95% of the jets in the event; the cases where an ambiguous association was made occured when the jets produced by two partons merged into one jet cluster.

The jet energy resolution for the relatively low energy jets in these events is influenced by several factors:

- the resolution of the calorimeter;

- the magnetic field sweeping low-energy charged particles out of the jet cluster cone;
- the thresholds used to detect energy in the calorimeter;
- the algorithm used to define jet clusters; and
- the association of energy with the jet that comes from either the underlying event or other jet fragments.

We show in Fig. 7(a) and (b) the fraction of the generated parton's energy that was not found in the jet cluster for jets with measured $E_T < 50$ GeV and measured $E_T > 50$ GeV, respectively. Both distributions show that $\sim 20 - 30\%$ of the jet energy is not found as clustered energy and more importantly the spread in this loss is of order 15-20%. The tail in Fig. 7(b) due to jets that have more energy than the generated parton comes from clusters that result from two nearby partons fragmenting to yield one cluster (those clusters typically have high E_T's and so show up preferentially in the latter distribution). The shoulder in each distribution near zero is due to jets that have hard fragmentations or that fragment predominantly into electromagnetic energy.

We have not investigated in detail the individual sources of energy loss. However, we have considered the effect higher tower E_T thresholds would have on the jet energy resolution. We show in Fig. 8 the effect of using total E_T tower thresholds of 0.5 and 1.0 GeV on the observed cluster energies. We plot in those distributions the amount of observed energy that is found in a cone of $R = 0.5$ about the measured jet axis in towers with E_T below the two different thresholds, expressed as a fraction of the generated parton's energy. We see that for the low-energy jets, a tower E_T threshold of 1.0 GeV will cause the loss of $\sim 20\%$ of the parton's energy, and would introduce an additional smearing in the observed jet energy of about 10%. A tower E_T threshold of 0.5 GeV reduces this effect by a factor of ~ 2. We conclude from this that E_T tower thresholds on the order of 0.5 GeV or greater have a significant effect on the jet energy resolution.

To make a crude correction for the energy lost outside of the jet cluster in the subsequent jet studies, we added 9 GeV of energy to the measured E_T of the jet clusters and scaled their momenta accordingly. The amount of energy added was chosen by simply considering the mean amount of energy missing in the jet clusters. We show in Fig. 9(a) the difference between the corrected and generated E_T of the partons resulting from the $W \to q\bar{q}$ decay in this sample of events; the correction has approximately centered this distribution.

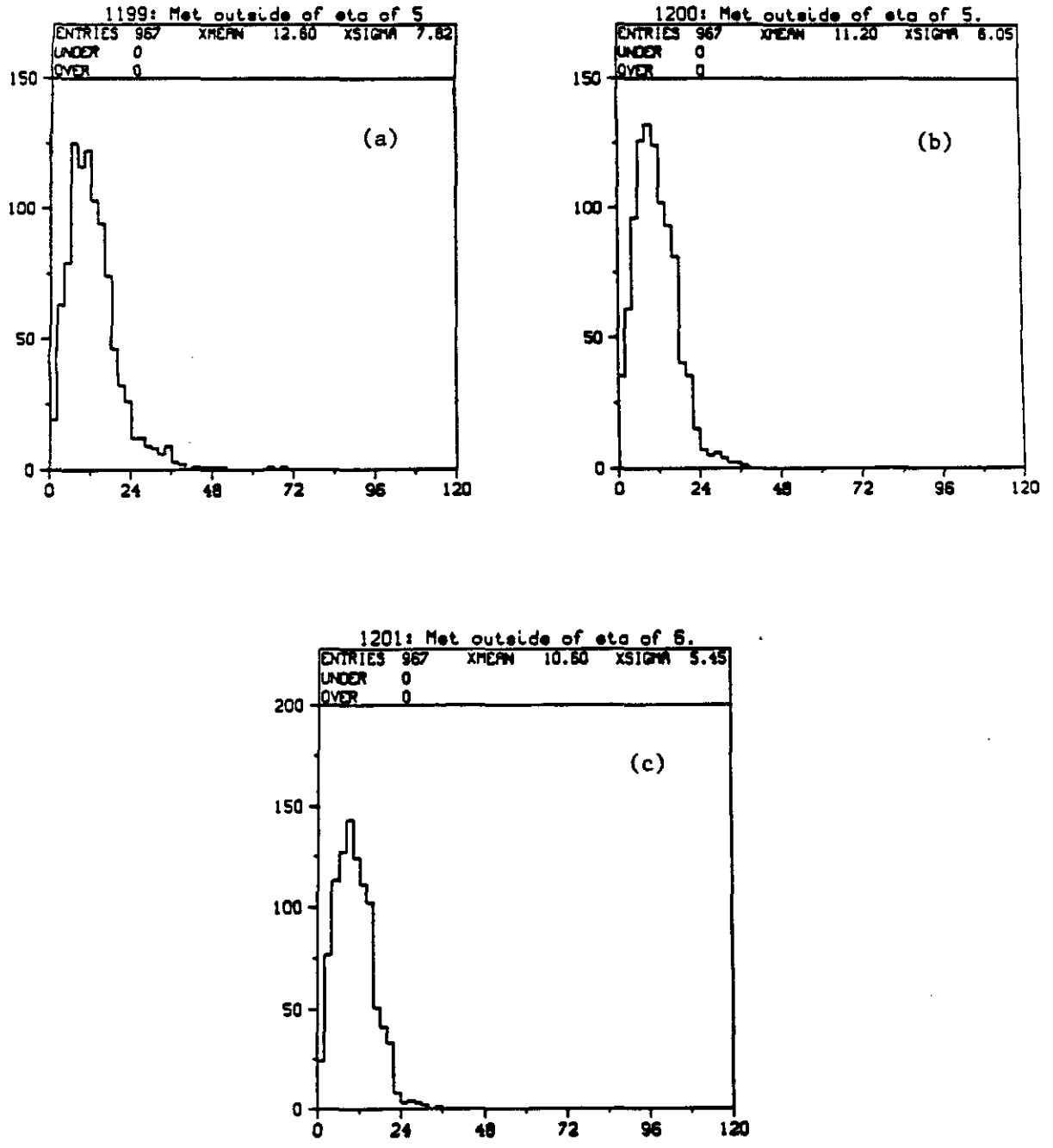

Figure 5: The distributions of the magnitudes of the transverse component of the summed vector E_T for particles with $|\eta| > 5.0$, $|\eta| > 5.5$ and $|\eta| > 6.0$ are shown in (a), (b) and (c), respectively.

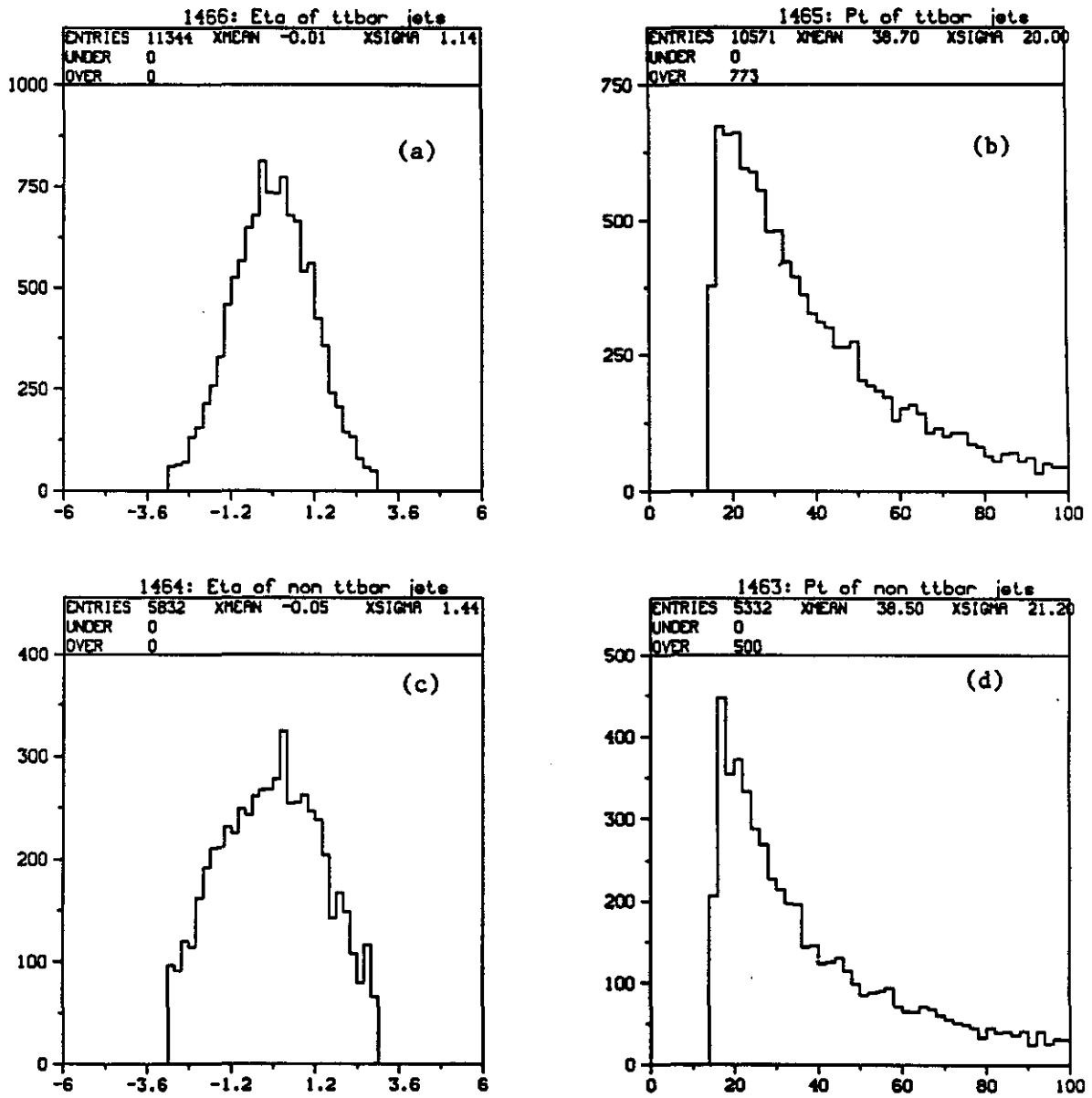

Figure 6: The η and E_T distribution of the jets passing the jet selection from the $t\bar{t}$ system are shown in (a) and (b), respectively. The comparable distributions for jets not generated by the $t\bar{t}$ decay products are shown in (c) and (d).

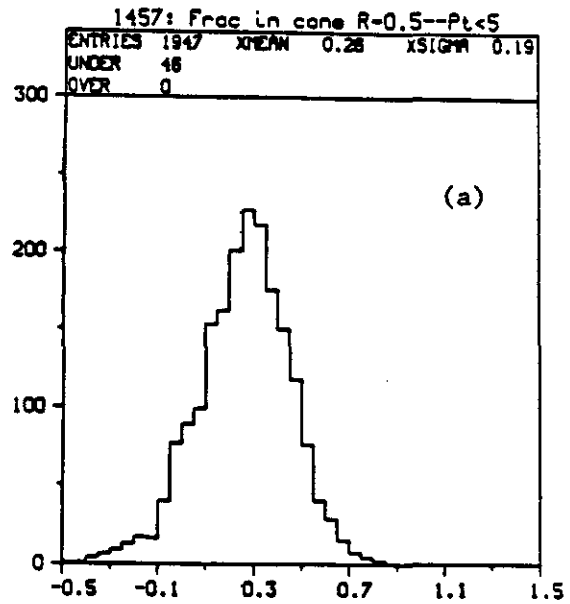

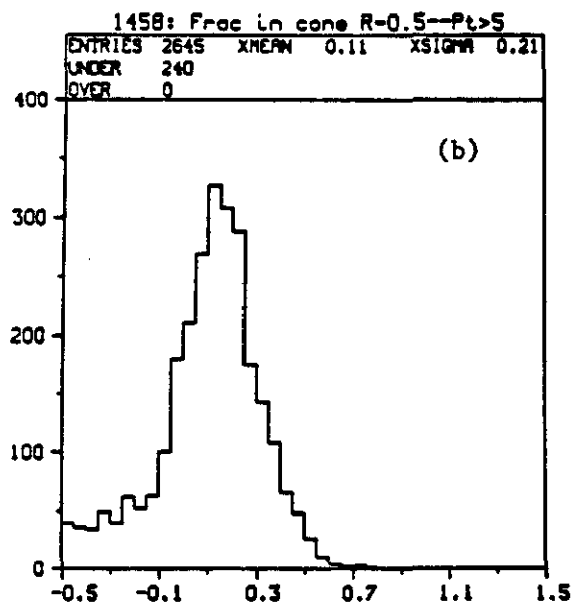

Figure 7: The distribution of the energy not associated with the jet cluster, as a fraction of the original parton energy, for jets with measured $E_T < 50$ GeV (a) and $E_T > 50$ GeV (b).

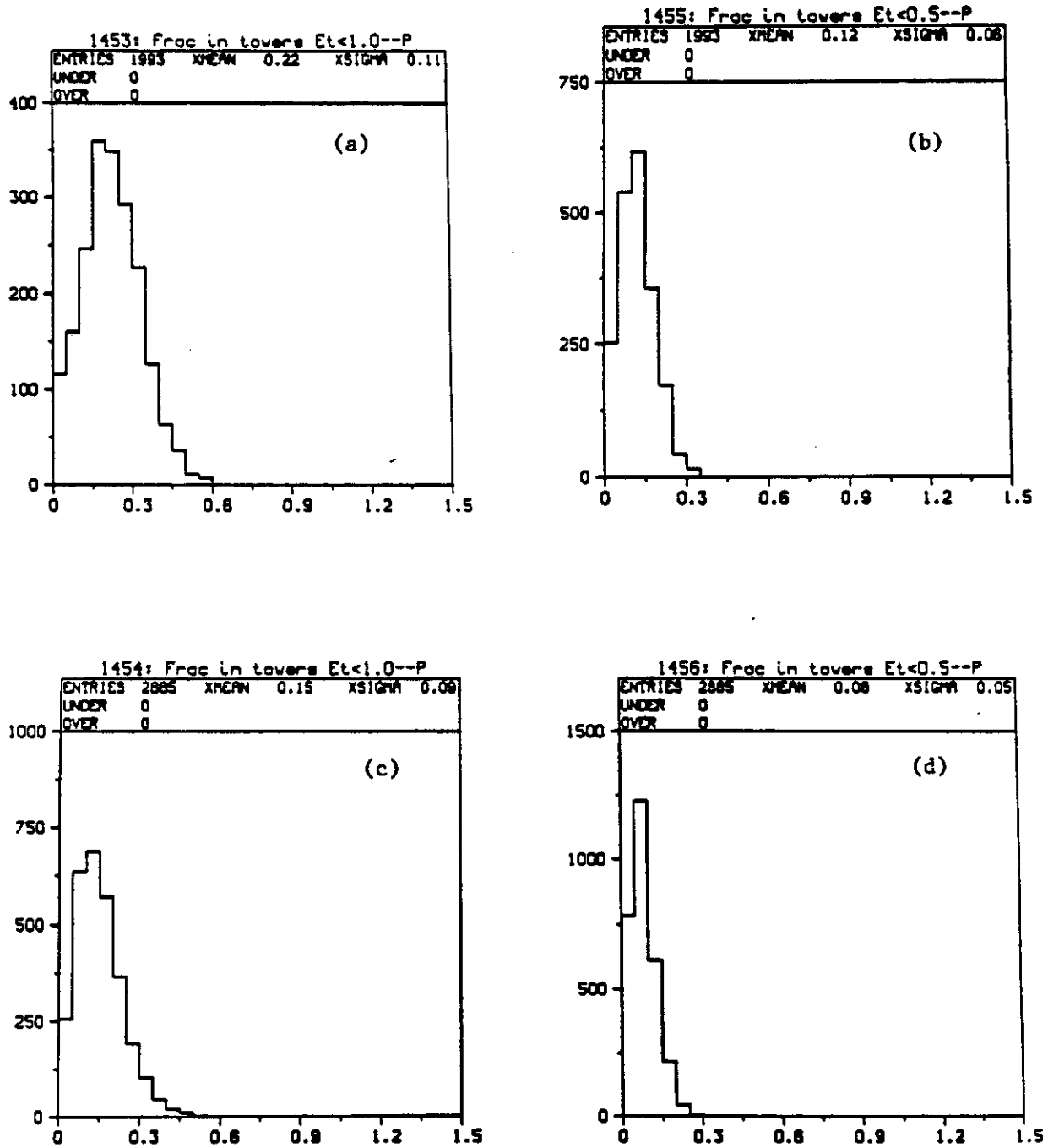

Figure 8: The distribution of the amount of observed energy that is found in a cone of $R = 0.5$ about the measured jet axis in towers with E_T below 1.0 and 0.5 GeV in (a) and (b) for jets with measured $E_T < 50$ GeV, expressed as a fraction of the generated parton's E_T. The comparable plots for jets with measured $E_T > 50$ GeV are shown in (c) and (d).

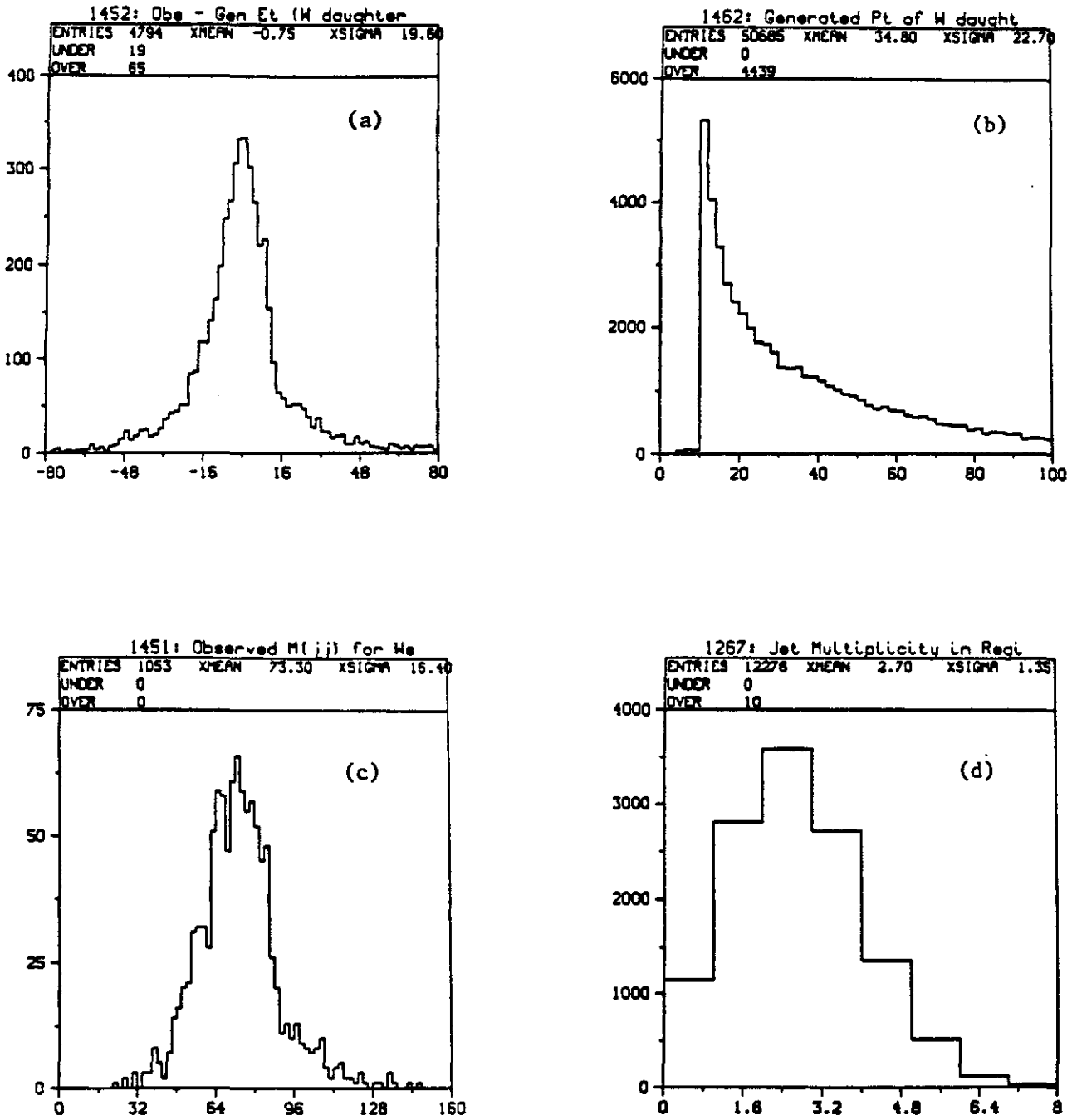

Figure 9: The distribution of the difference between the measured jet E_T (after the correction discussed in the text) and the generated parton associated with the jet for jets resulting from the hadronic decay of the W is shown in (a). The generated P_T spectrum of the W daughters is shown in (b). The dijet invariant mass spectrum for the reconstructed jet pairs resulting from the W decay daughters is shown in (c). The jet multiplicity distribution for the events satisfying the electron and neutrino selection is shown in (d).

4.4 Further Jet Selection

We show the jet multiplicity distribution for the ~12 300 events passing the electron and neutrino selection in Fig. 9(d). To reduce the large expected backgrounds from other sources of inclusive $W \rightarrow e\nu_e$ events, we selected only those events that had at least three jet clusters satisfying the jet requirements discussed in the previous section. There are 4756 events that survive this selection (39%).

4.5 $W \rightarrow q\bar{q}$ Reconstruction

We expect the primary background in this event sample to be due to $W+ \geq 3$ jet production. To provide rejection against this background, it is necessary to reconstruct the $W \rightarrow q\bar{q}$ final state using the observed jets. The signal we are looking for is shown in Fig. 9(c) where we have plotted the di-jet invariant mass, M^{jj}, of the pair of jets in each event that come from the hadronic decay of the second W boson. The width of this distribution is about 16 GeV/c^2 and it is displaced somewhat below the generated W mass of 80.5 GeV/c^2. We believe the displacement is a result of our incomplete jet energy correction, as well as the effect of final state radiation creating W final states where a significant fraction of the energy has not been included in the two jet clusters used to form this invariant mass.

One of the primary difficulties in extracting this signal from the data is the large combinatorial background that results if one includes all pairs of jets in the event to form a dijet invariant mass distribution, as is illustrated in Fig. 10(a) where we show the dijet invariant mass distribution for all pairs of jets in these events. This combinatorial background arises not just from jets resulting from the $t\bar{t}$ decay, but also from jets due to initial or final state radiation; we found that $\sim 1/3$ of the jets in these events are not $t\bar{t}$ decay products.

There are several ways of reducing this combinatorial background, one of which is to demand that the P_T of the dijet system, P_T^{jj}, be above some minimum value. This is motivated by the fact that in these events the W bosons are typically produced with a substantial amount of transverse energy. We show in Fig. 10(b)-(d) the M^{jj} distribution requiring $P_T^{jj} > 60$ GeVc, $P_T^{jj} > 120$ GeV/c and $P_T^{jj} > 180$ GeV/c, respectively. We see that the expected signal begins to rise above the background once we have required $P_T^{jj} > 120$ GeV/c, and it is quite apparent once we have required $P_T^{jj} > 180$ GeV/c.

The peak in Fig. 10(d) consists of ~ 100 events above a combinatorial background of order 50 events. This corresponds to an observed signal rate of ~ 15 pb. This is substantially larger than the expected rate from WW production alone. We have not estimated the size of the combinatorial backgrounds from inclusive W production. We believe on naive rate considerations alone that these may not be large, but a detailed calculation is necessary to

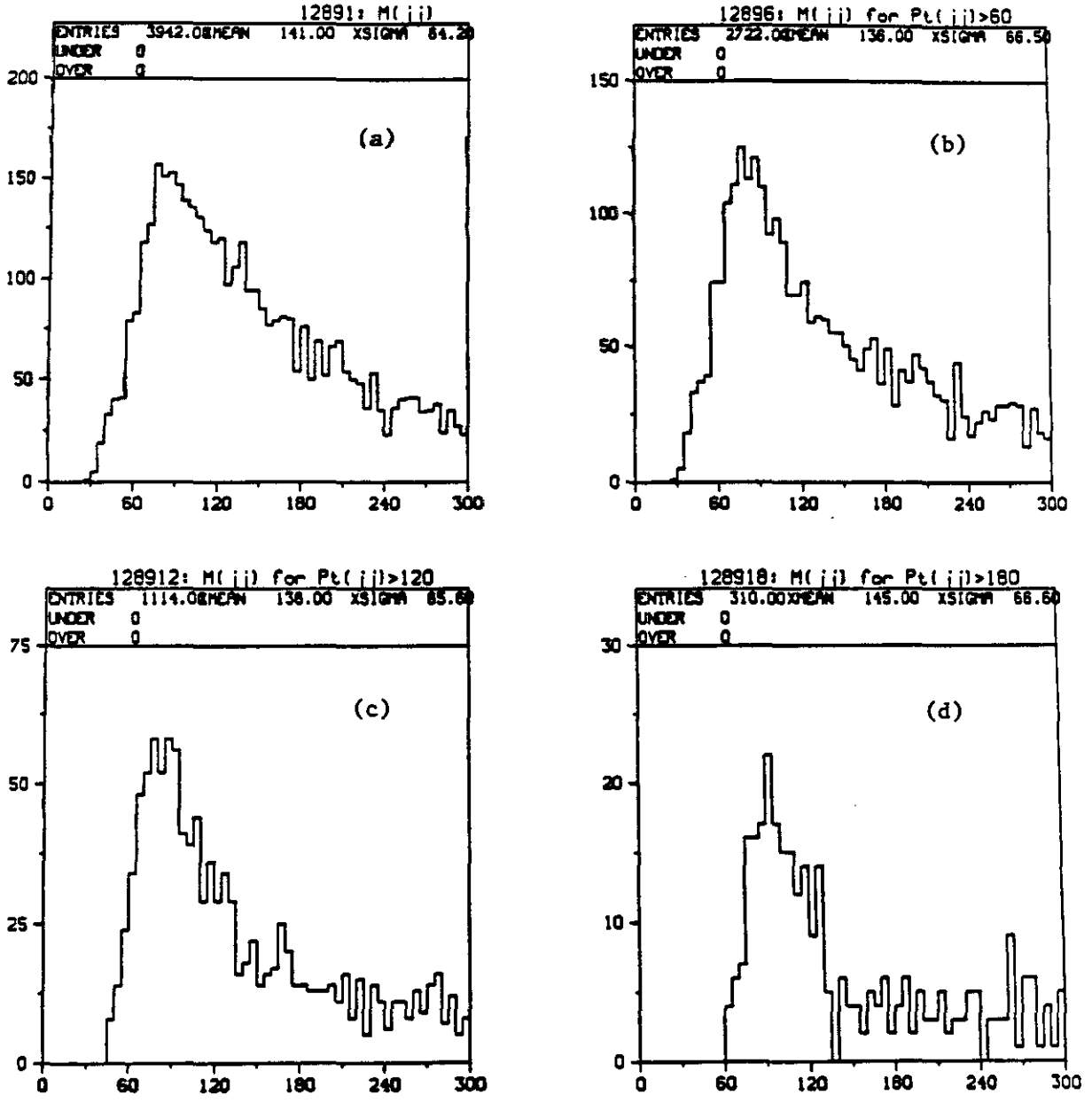

Figure 10: The M^{jj} distribution for all jet pairs (a), and pairs with $P_T^{jj} > 60$ GeVc, $P_T^{jj} > 120$ GeV/c and $P_T^{jj} > 180$ GeV/c in (b), (c) and (d), respectively.

answer this question.

We would also like to point out that this method for reconstructing the W mass is sensitive to the mass of the top quark. For a top quark mass of 150 GeV/c^2, the relativistic boost of the W boson from the top quark decay frame to the lab frame prefers to give the W boson most of the P_T of the top quark, which is why our simple selection works as well as it does. For heavier top quark masses, the b quark jets become on average more energetic and are more readily confused with the decay products of the W decay.

For example, we have performed a similar analysis for a top quark mass of 200 GeV/c^2 and have found that it is necessary to make more stringent requirements on the jets in order to see a clear W boson peak.

4.6 $t\bar{t}$ Event Reconstruction

One goal of our study was to see how difficult it would be at completely reconstruct $t\bar{t}$ events. Having successfully reconstructed the $W \to q\bar{q}$ system recoiling against the $W \to e\nu_e$ decay, we can now attempt to fully reconstruct the top quark producing the hadronically decaying W boson by including the b quark decay products. The combinatorial backgrounds are still rather large as there are typically several candidate b quark jets remaining in each event.

To overcome this problem, we assume that the detector has the ability to tag some reasonable fraction of the b quark jets, using, for example, the presence of a secondary vertex and/or a lepton inside the jet cluster. We therefore consider all pairs of jets in the events that have $M^{jj} < 135$ GeV/c^2 and combine the resulting dijet system with a tagged b quark jet to form the three-jet invariant mass, M^{jjb} (we identify the b quark jets using the generated parton information). This mass distribution is shown in Fig. 11(a). Although this distribution peaks at approximately the generated mass of the top quark, this peaking is a kinematical effect and is not evidence of a real signal.

Since we know that with random pairings of jets, the W boson is not correctly reconstructed a large fraction of time unless we require the dijet system to have a significant amount of P_T, we therefore make a similar requirement now by requiring the P_T of the three-jet system, P_T^{jjb}, to be large. The M^{jjb} distributions for the three-jet systems that have $P_T^{jjb} > 60$ GeV/c, $P_T^{jjb} > 120$ GeV/c and $P_T^{jjb} > 180$ GeV/c are shown in Fig. 11(b), (c) and (d), respectively. We see that a signal slightly below the 150 GeV/c^2 mass of the top quark appears above the combinatorial background. For the very highest P_T^{jjb} selection, a mass peak of approximately 50 events is evident, which corresponds to a rate of ~ 10 pb. This rate assumes a 100% efficiency for tagging the b quark once the b quark jet has been reconstructed. A more reasonable estimate of this efficiency may be 10%, which still yields a rate of ~ 1 pb, corresponding to $\sim 10\,000$ observed events/SSC year (1 SSC year $\equiv 10^{40}$

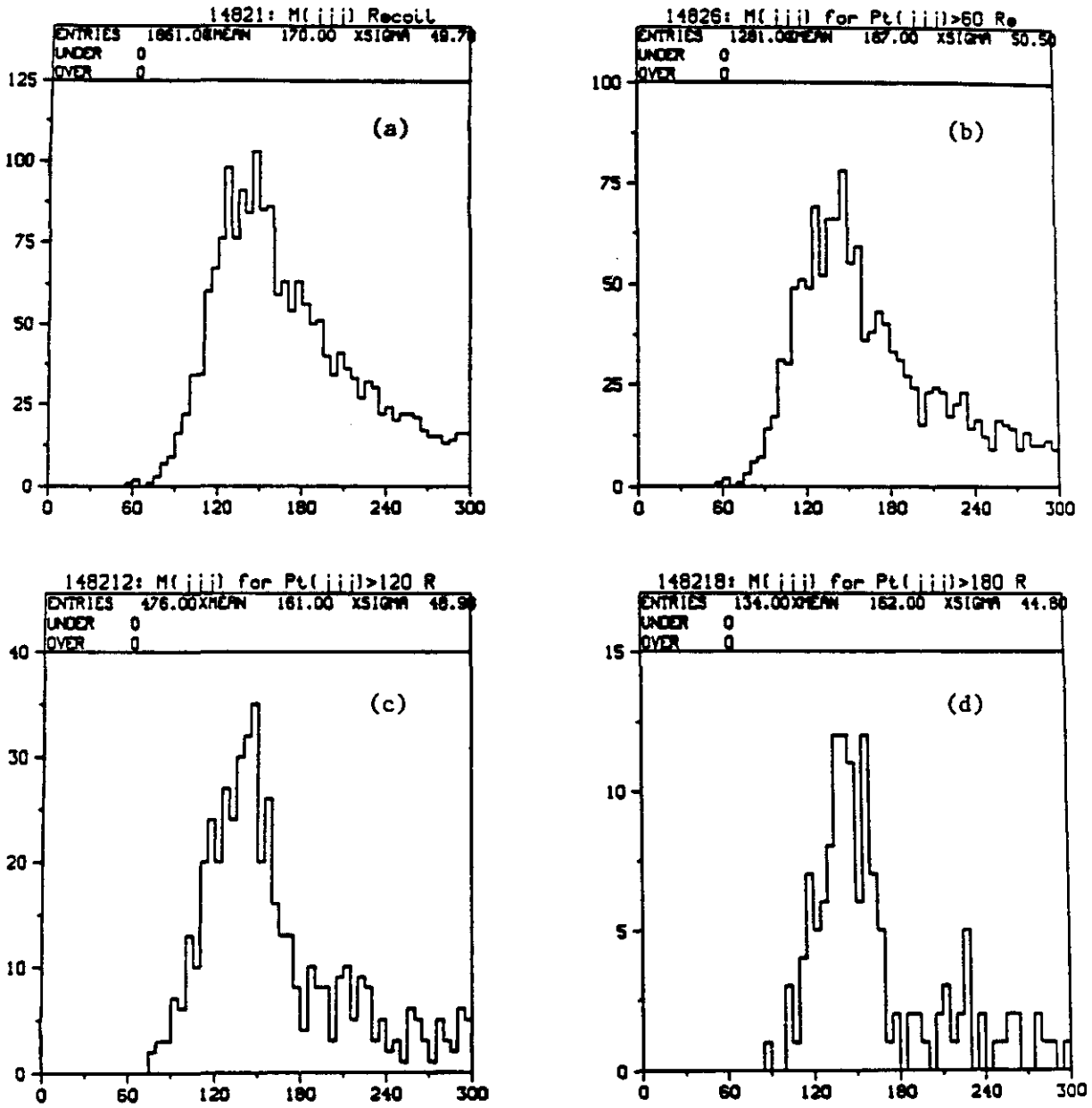

Figure 11: The M^{jjb} distribution for all combinations of jet pairs and b quark jets (a), combinations with $P_T^{jjb} > 60$ GeVc, $P_T^{jjb} > 120$ GeV/c and $P_T^{jjb} > 180$ GeV/c in (b), (c) and (d), respectively.

cm^{-2}).

Although this reconstruction strategy is by no means optimal, it demonstrates that it is possible to reconstruct the full hadronic decay modes of the top quark in the case where the other top quark has decayed semi-leptonically. This means that we can make a direct measurement of the top quark mass, one of the few remaining unknown parameters in the standard model.

We would also like to point out that the efficacy of this search strategy varies with M_{top}. As the top quark mass increases, the b quark jets in the event increase in P_T more rapidly than do the jets from the W decay. The net result is that it is harder to disentangle the jets in the event, but it is easier to find the b quark jets. On the other hand, the W signal in the dijet mass spectrum is easier to resolve for lower top quark masses, but the b quark jets are somewhat more difficult to reconstruct, as they tend to have even lower P_T's. In either case, we believe that it will be possible to reconstruct fully-hadronic top quark decays, but more study is required to substaniate this point.

4.7 Effect of Poorer Calorimeter Resolution

We performed the same analysis on the $t\bar{t}$ sample processed with the degraded calorimeter response dicussed in Sec. 4.2. The comparable M^{jj} and M^{jjb} distributions are shown in Fig. 12 and Fig. 13. The resulting top quark signal appears to be somewhat less pronounced but a clear peak is still visible.

5 Effect of Multiple Interactions

Due to the high SSC luminosities, we expect a mean of 1.6 interactions per bunch crossing in the detector, which causes "pileup" of events in the detector. This effect is further magnified in the cases where the calorimeter readout takes place over a time interval that is several bunch crossings long. Hence, the information collected in the calorimeter may be degraded by the overlap of several "minimum-bias" events on top of the high P_T collision that created the $t\bar{t}$ final state. The isolation of the electron shower in the calorimeter has been thought to be a quantity sensitive to event pileup. However, pileup also will affect the amount of energy from the underlying events that is associated with a jet cluster and so one should expect to see some degradation in the jet energy and $\not{E}_T$ resolution.

5.1 Model Used for Pileup

We created a sample of "minimum-bias" events by using the ISAJET 6.22 Monte Carlo to generate 10 000 TWO JET events, with jet P_T in the range 5-20 GeV/c. We then simulated

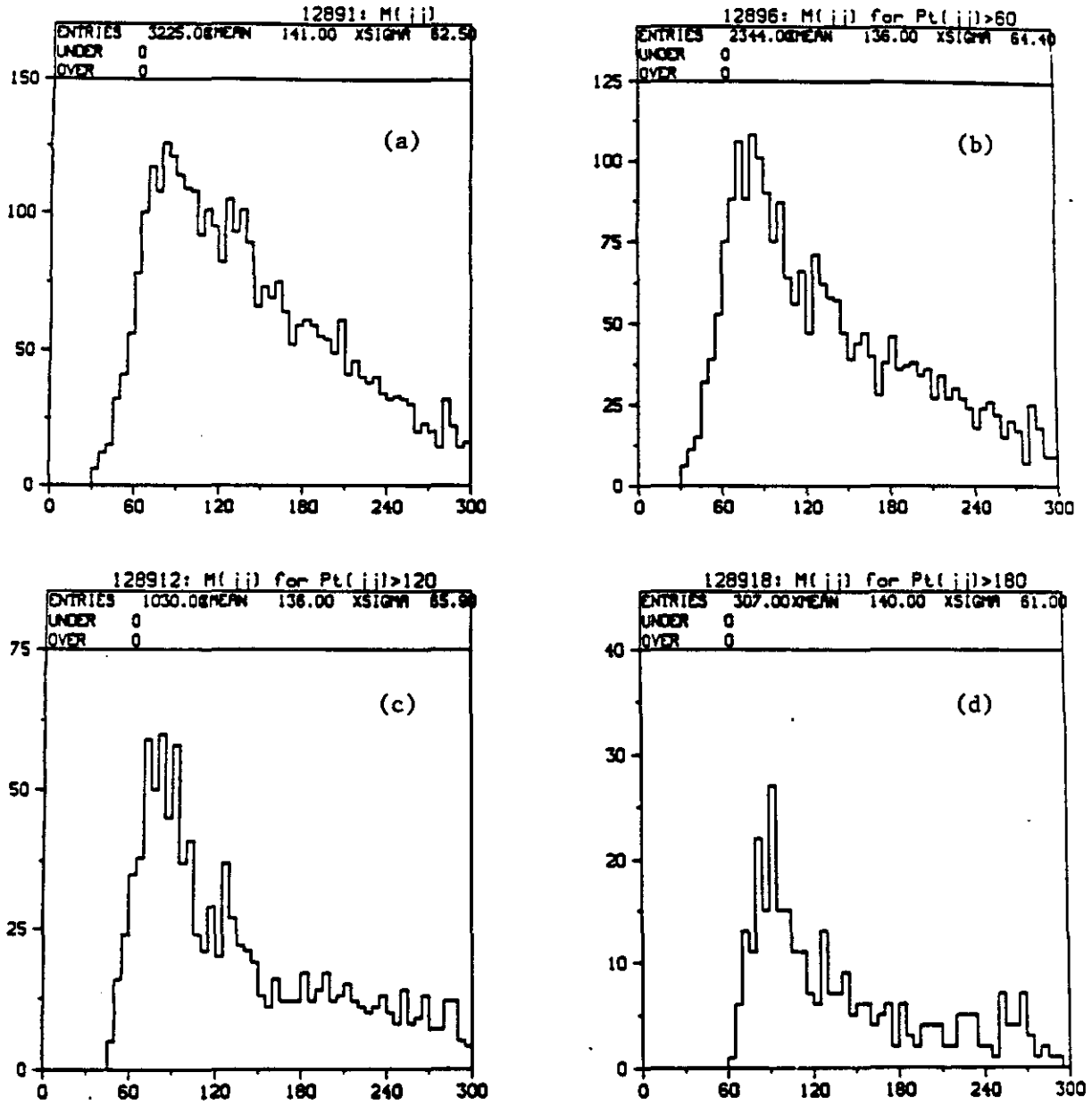

Figure 12: The M^{jj} distribution for all jet pairs (a), and pairs with $P_T^{jj} > 60$ GeVc, $P_T^{jj} > 120$ GeV/c and $P_T^{jj} > 180$ GeV/c in (b), (c) and (d), respectively, using the degraded calorimeter performance.

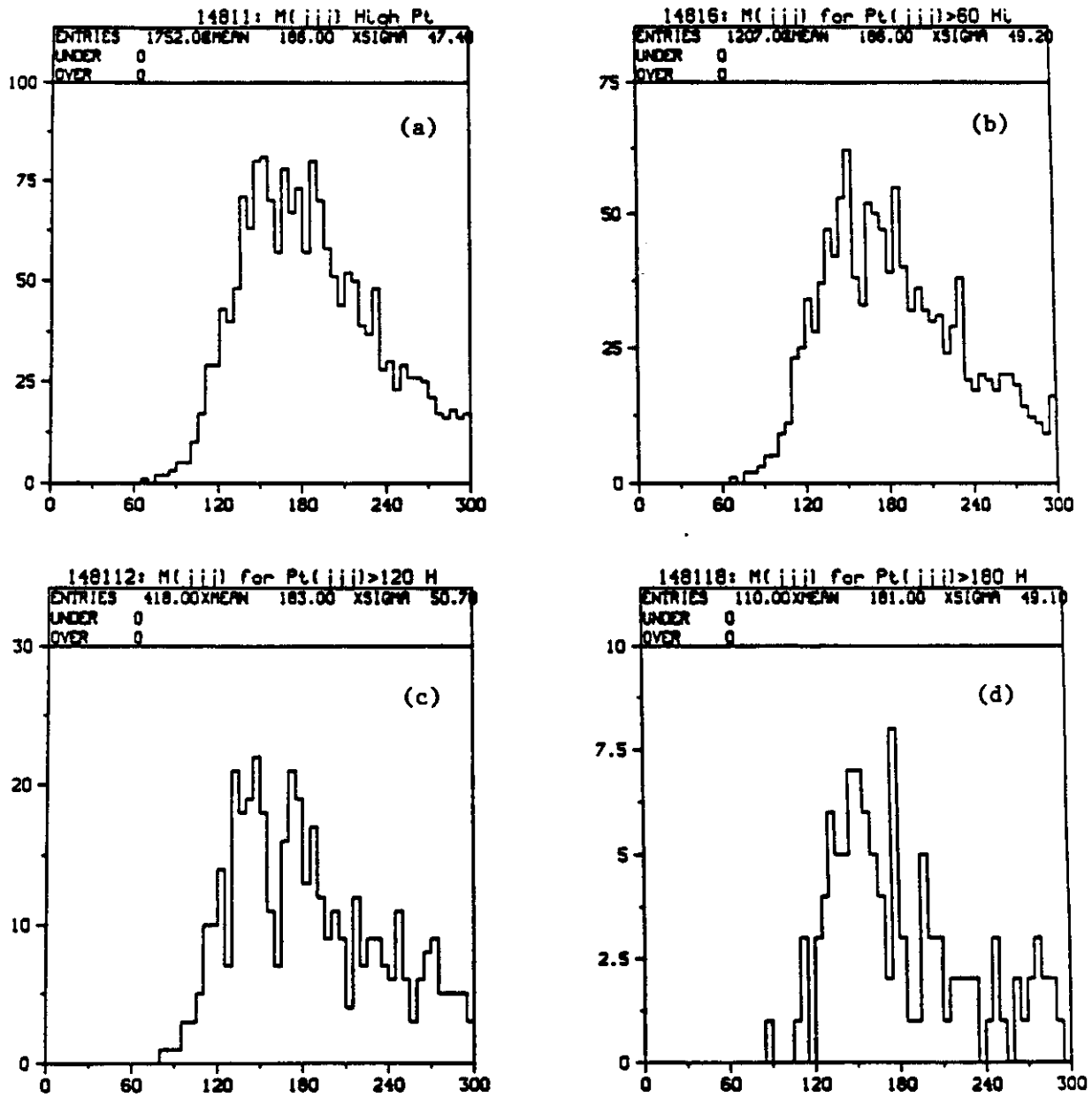

Figure 13: The M^{jjb} distribution for all combinations of jet pairs and b quark jets (a), combinations with $P_T^{jjb} > 60$ GeVc, $P_T^{jjb} > 120$ GeV/c and $P_T^{jjb} > 180$ GeV/c in (b), (c) and (d), respectively, using the degraded calorimeter performance.

the calorimeter response for each event. A number of these events were then added to the simulated calorimeter information resulting from the $t\bar{t}$ interaction depending on what we assumed about the calorimeter response as a function of time. We employed a model in which the detector was triggered on the crossing in which the $t\bar{t}$ interaction occured. The model then assumed that the calorimeter was sensitive to energy deposited some time before and after the trigger, with a response that could vary depending on the difference in time between the energy deposition and the trigger.

We investigated two different response functions:

- A "flat" response that was independent of the time difference between the energy deposition and the trigger.
- A "bipolar" response function, where we approximated the behaviour of a typical shaping circuit in a liquid-ionization calorimeter. The response function was equal to 1.0 for energy deposited at the time of the trigger and varied sinusoidally for interactions that occured up to 3/4 of a "shaping period" prior to the trigger and 1/4 of a shaping period after the trigger. Thus, for interactions that occured between 3/4 and 1/4 shaping period prior to the trigger, the response function was negative and any energy deposited in the calorimeter tower during that time period would reduce the total signal observed in that calorimeter channel.

We consider four different calorimeter responses: a flat response over a 100 ns interval, a flat response over a 200 ns interval, a bipolar response with a 100 ns shaping period, and a bipolar response with a 400 ns shaping period. To correctly account for the fluctations in the number of interactions per crossing, we determined the number of interactions by sampling from a Poisson distribution with a mean of 1.6 events for each crossing before or after the trigger for which the calorimeter had a non-zero response, We then multiplied the energy in each tower in the minimum-bias interactions occuring at that crossing by the calorimeter response function for that crossing and then added the resulting energy to the $t\bar{t}$ interaction, tower-by-tower. After all interactions had been added, the signals in towers with negative total energy were zeroed and the event was reconstructed as described earlier.

5.2 Effect on Lepton Isolation

We show in Fig. 14 the distribution for h/em, $E_T^{0.4}$ before and after the event selection, and E_T^{iso} before and after the event selection for the case when no multiple interactions were added (the event selection includes the $\not{E}_T$ and jet requirements). We then show the same electron isolation distributions for the case of a flat 100 ns response in Fig. 15, a flat 200 ns

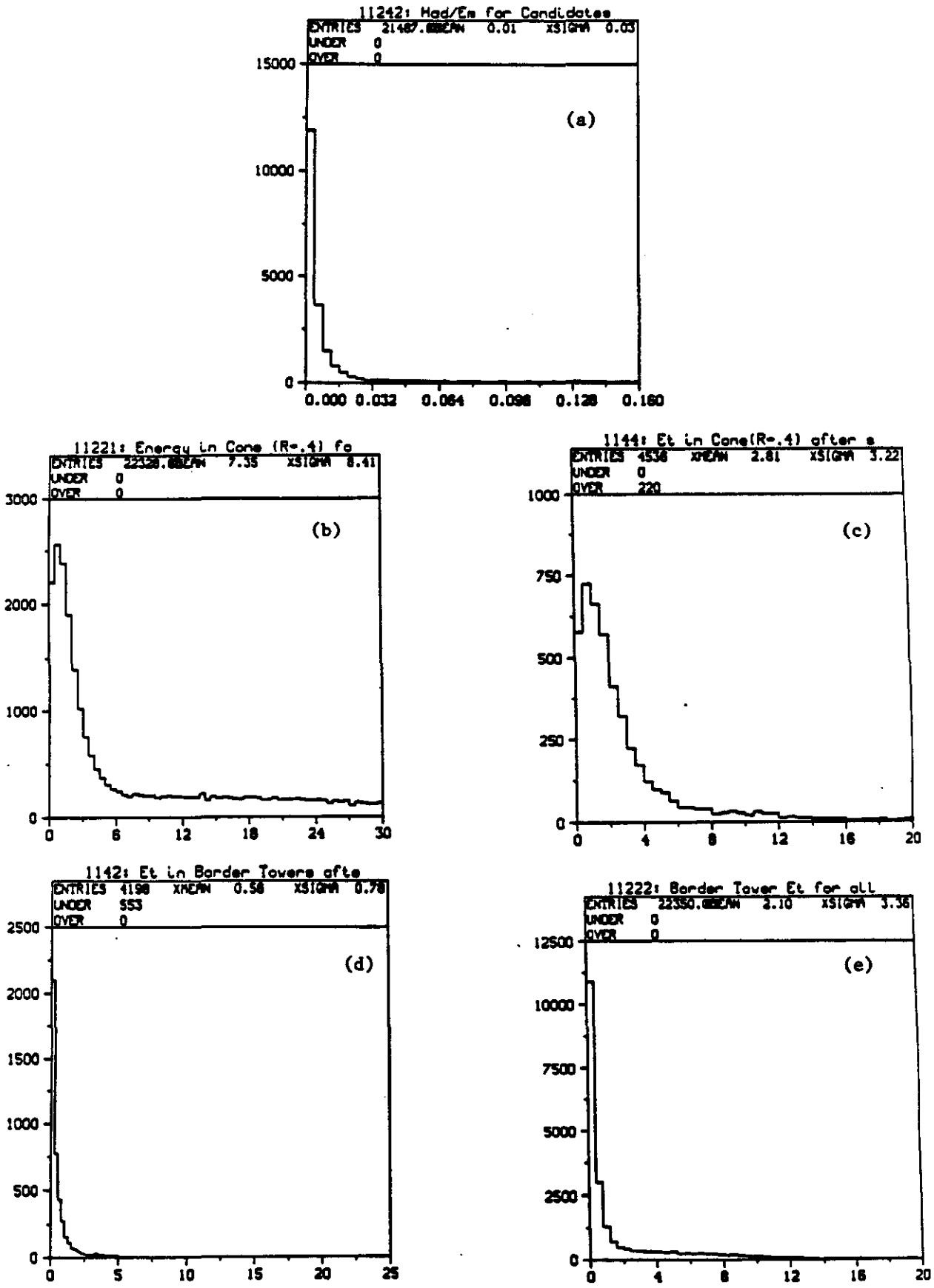

Figure 14: The distribution of h/em, $E_T^{0.4}$ before and after the event selection, and E_T^{iso} before and after the event selection for the nominal case where no multiple interactions have been added.

response in Fig. 16, a bipolar 100 ns response in Fig. 17, and a bipolar 400 ns response in Fig. 18.

We see that both the h/em and E_T^{iso} distributions are the least sensitive to the effects of multiple interactions, which is as expected since these are the most local isolation variables considered. For example, the average E_T^{iso} after the selection (where we have required $E_T^{iso} < 5$ GeV) goes from 0.51 GeV in the case of no multiple interactions to 1.31 for a flat 200 ns response function, which is the worst case of the four we considered (the pessimist may correctly argue that this reduces the rejection of this variable by a factor of two since one now has to cut at a much larger E_T^{iso} value to retain the same signal efficiency). The energy within the cone of $R = 0.4$ is clearly most affected by the inclusion of multiple interactions; the entire distribution is displaced by about 6 GeV and is substantially broader when a flat 200 ns response is assumed.

It is interesting to note the effect the bipolar shaping response has on the observed lepton isolation. We see essentially no pileup effect in the case where we have assumed a 100 ns bipolar shaping period. The mean $E_T^{0.4}$ for the events after selection increases from 2.8 GeV without multiple interactions to 5.1 GeV when a 400 ns bipolar shaping response is used to model the behaviour of the calorimeter readout. This is substanitally smaller than the mean of 8.0 that results from having a flat 200 ns gate and is almost comparable to the effect of a 100 ns flat response (mean of $E_T^{0.4}$ is 4.6 GeV). Perhaps even more interesting is the fact that the width of the resulting isolation distribution is narrower in the case of the bipolar response, presumably due to the larger number of energy depositions one is averaging over in the case of a long shaping period.

From these comparisons, we conclude that the signal processing characteristics of the calorimeter front end play a significant role in determining the overall effect multiple event pileup has on the physics capabilities of the detector. We also conclude that even a flat 100 ns response does not wreak great havoc with the ability of the calorimeter to detect isolated leptons. We should note, however, that at a factor of 10 higher luminousities one may no longer be able to measure lepton isolation using the calorimeter information, even if one has a calorimeter that was sensitive to only a few crossings around which the trigger occurs.

5.3 Effect of Pileup on Selection Efficiency

Although our electron selection is based almost entirely on a local isolation criteria, we found that the the fraction of electron candidates with $E_T > 20$ GeV and $|\eta| < 3$ that survived the h/em and E_T^{iso} cuts did not vary more than a few percent when the different pileup scenarios were simulated (the efficiency of these two cuts was typically 67%). However

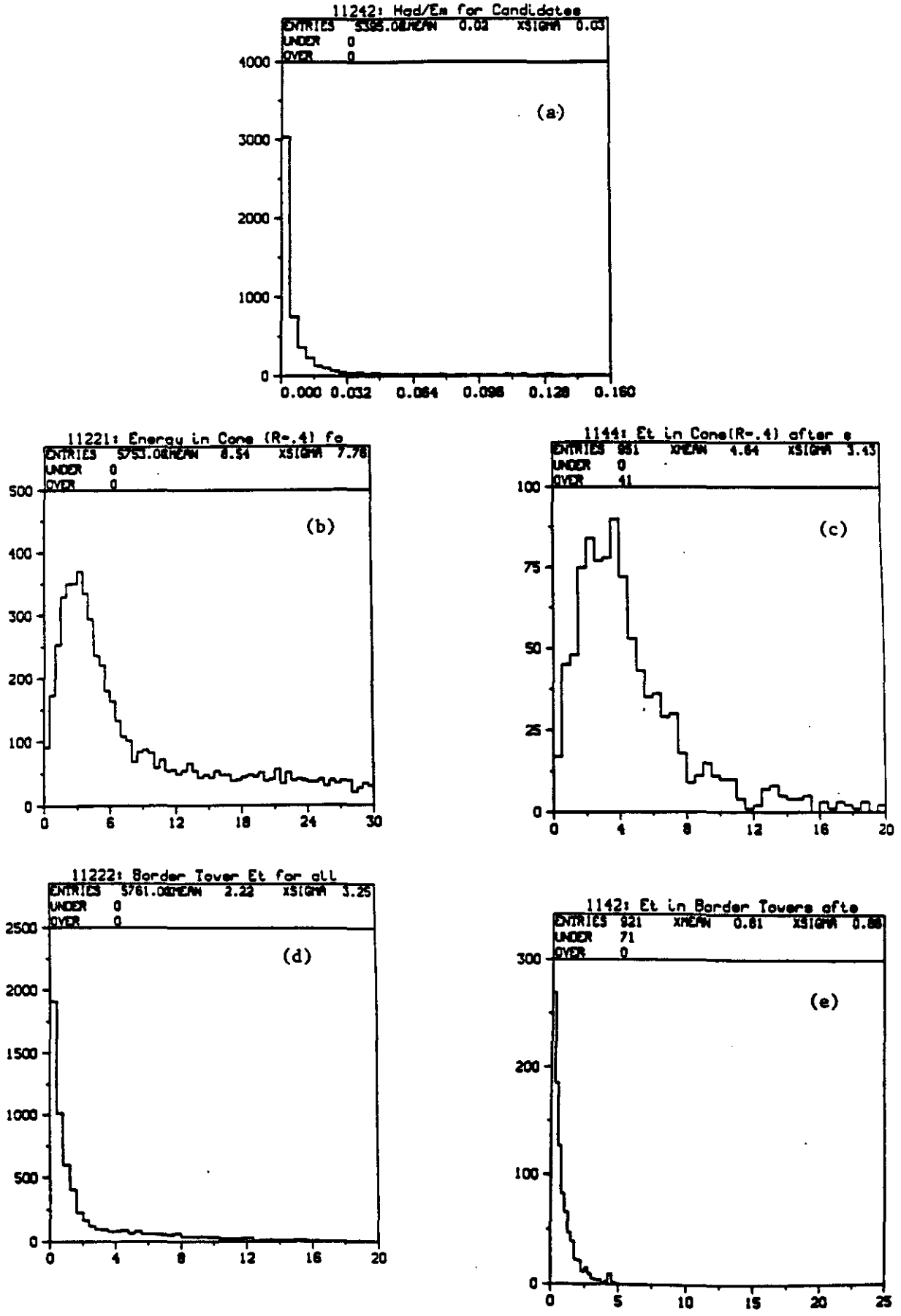

Figure 15: The distribution of h/em, $E_T^{0.4}$ before and after the event selection, and E_T^{iso} before and after the event selection for a calorimeter with a flat 100 ns response function.

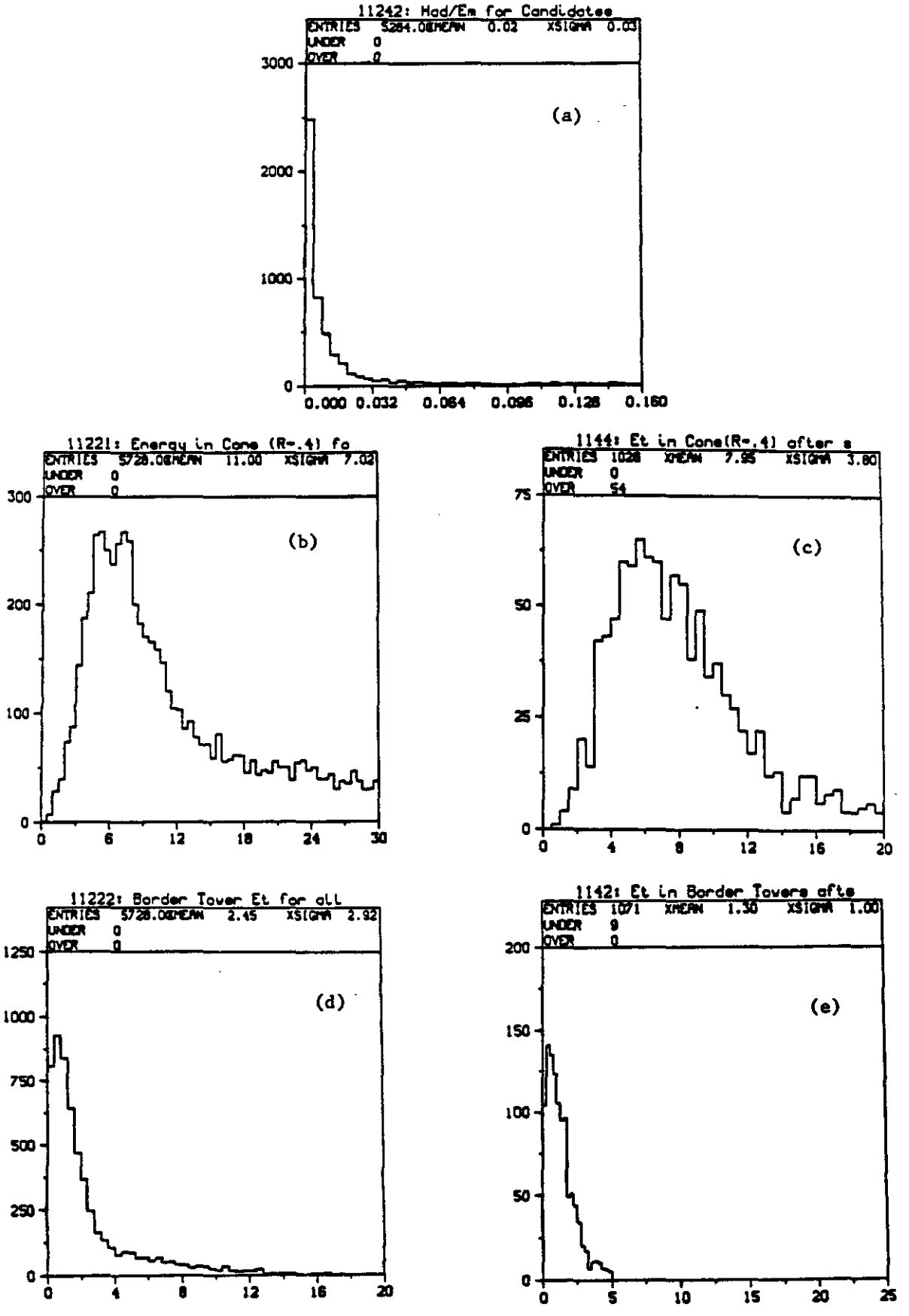

Figure 16: The distribution of h/em, $E_T^{0.4}$ before and after the event selection, and E_T^{iso} before and after the event selection for a calorimeter with a flat 200 ns response function.

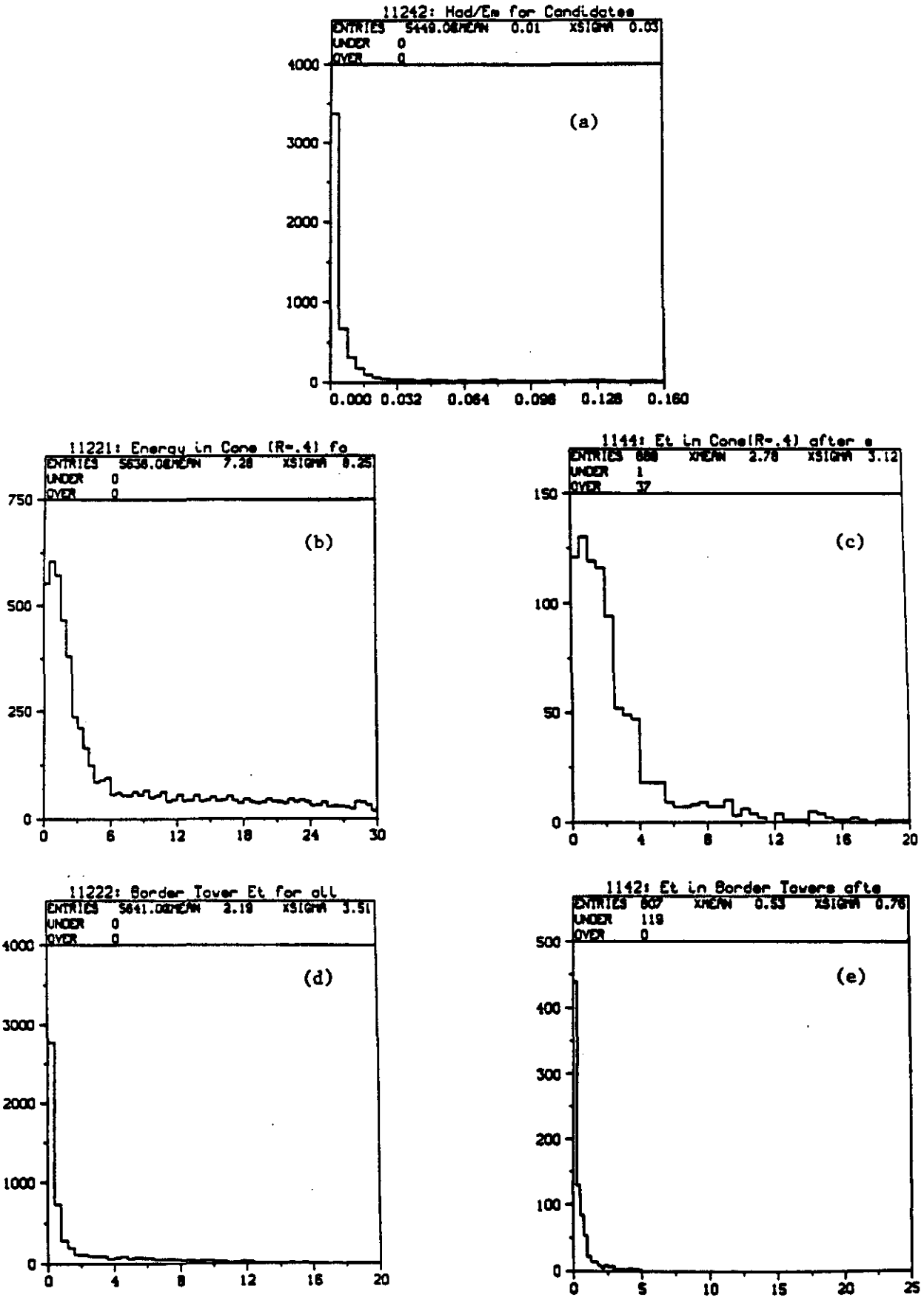

Figure 17: The distribution of h/em, $E_T^{0.4}$ before and after the event selection, and E_T^{iso} before and after the event selection for a calorimeter with a bipolar 100 ns response function.

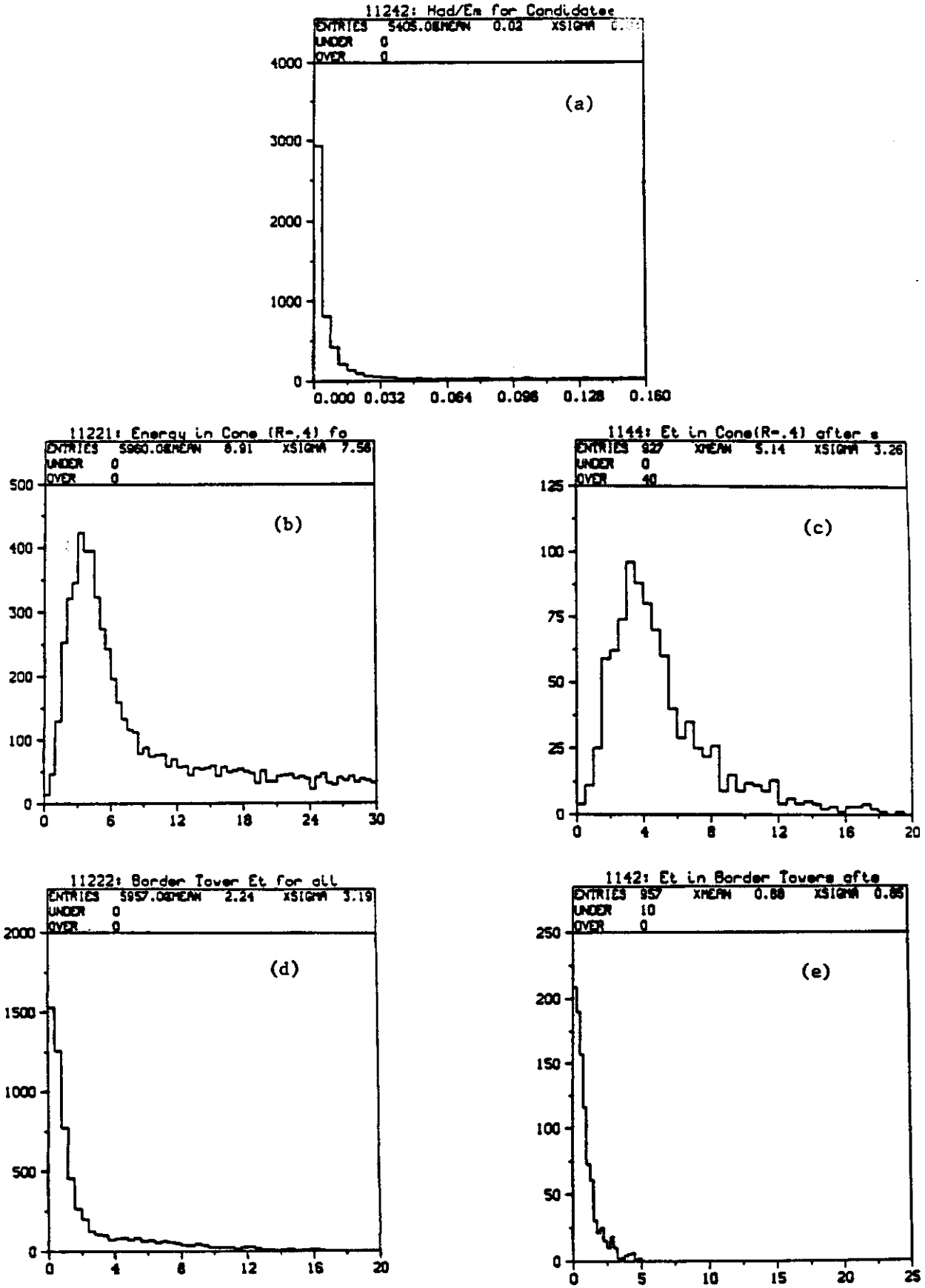

Figure 18: The distribution of h/em, $E_T^{0.4}$ before and after the event selection, and E_T^{iso} before and after the event selection for a calorimeter with a bipolar 400 ns response function.

this reflects the fact that our E_T^{iso} and h/em requirements were rather loose. We show in Fig. 19 the fraction of electrons that survive the E_T^{iso} cut as a function of the E_T^{iso} cut for the different pileup scenarios. From these efficiency curves, we see that the efficiency of an E_T^{iso} cut of 1.5 GeV varies from about 90% to 65-70% over the different scenarios.

How important this is depends on the rejection needed to eliminate the backgrounds from non-isolated electrons in the analysis (which have approximately flat E_T^{iso} distributions for these values of E_T^{iso}). Although we have not studied the SSC background rates in detail, CDF has found that the backgrounds from non-isolated electrons have been manageable for these high-P_T leptons [11]. For example, it may be acceptable to reduce the severity of the E_T^{iso} cut to remain efficient even at the cost of a factor of two or three in rejection.

However, this does not directly address what effect pileup has on the electron identification efficiency. Most electron identification schemes suffer some degradation in efficiency when the electron candidate is not locally isolated. Since the h/em and E_T^{iso} distributions are relatively insensitive to pileup, this indicates that the overall electron ID efficiency may not suffer much degradation due to pileup. However, a detailed study would have to be performed to verify this for a given electron ID scheme.

6 Summary and Conclusions

We have studied some of the issues associated with the detection of a top quark with a mass of 150 GeV/c^2, using a relatively simple model of an SSC calorimeter. We have shown that it is possible to fully reconstruct a $t\bar{t}$ event in the case where one top quark decays semi-leptonically and the other hadronically using the electron and $\not{E}_T$ signature, reconstructing the $W \rightarrow q\bar{q}$ and tagging the jet from the associated b quark. This method should provide sufficient rejection against the inclusive W backgrounds, although we have not completed a detailed calculation to verify this.

We have also found the electron candidates in these events to be typically well isolated. The effect of multiple interaction pileup in the calorimeter has been modelled using several different calorimeter responses functions. In the worst scenarios, the local lepton isolation is degraded by a factor of two, while more non-local isolation measures are more significantly affected.

The $\not{E}_T$ resolution does not appear to be dominated by the calorimeter energy response at the ν_e energies characteristic of this process. The effect of additional ν's in the event appears to be the most significant source of $\not{E}_T$ smearing. It also appears that extending the η coverage beyond ± 5 will not have a profound effect on the $\not{E}_T$ resolution for this signal. We have found that the energy resolution of jet clusters using a relatively simple clustering

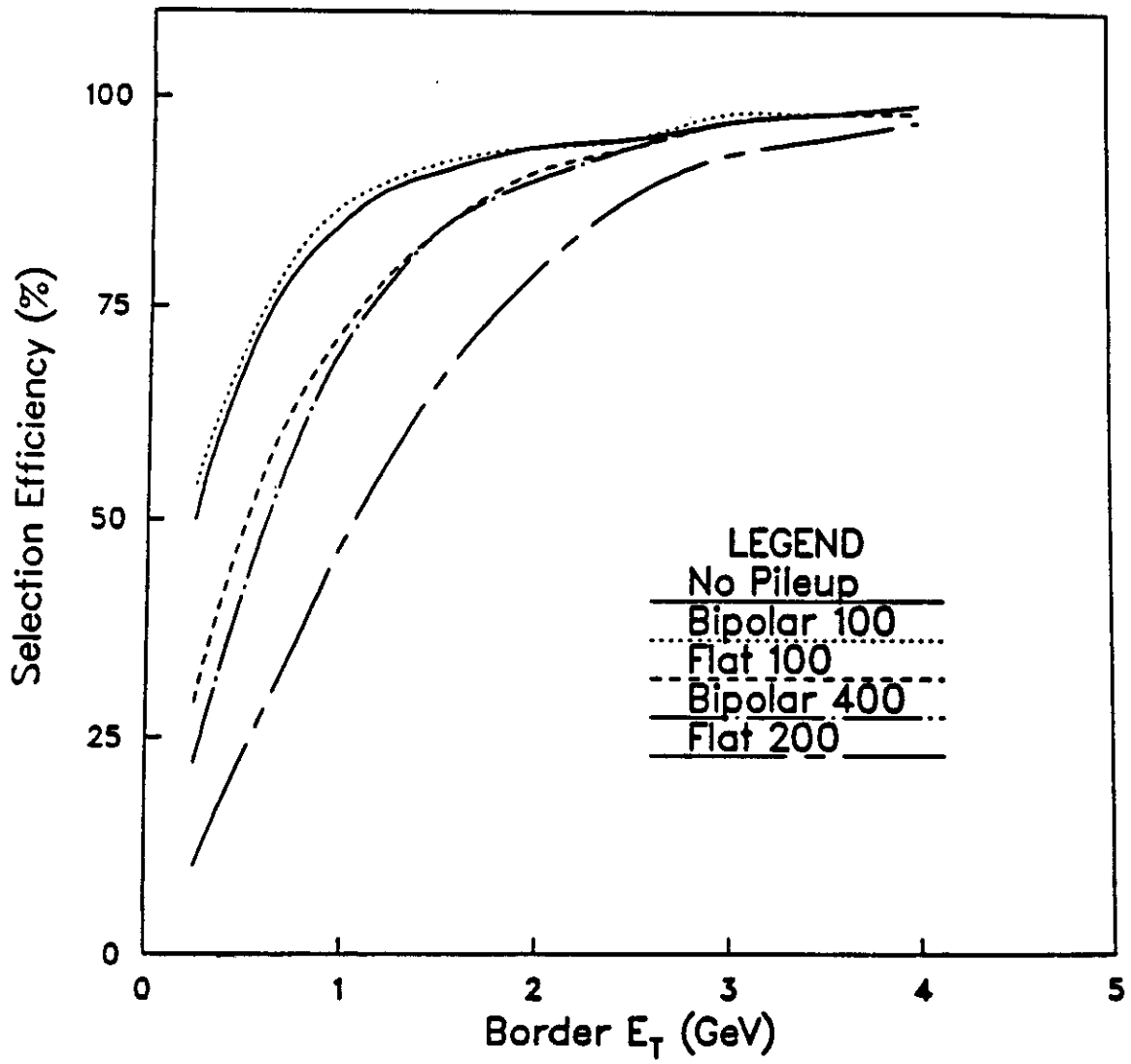

Figure 19: The efficiency of the E_T^{iso} cut for electrons with $E_T >$ 20 GeV and $|\eta| < 3$ for the different event pileup scenarios. (The E_T^{iso} distribution resulting from the 100 ns bipolar response is essentially indistinguishable from the nominal case with no pileup; their difference is due to statistical fluctuations in the distribution used to extract these curves.)

algorithm is adequate to perform the reconstruction of the hadronic decay of the top quark.

The calorimeter simulation employed in this study is relatively simple and does not include such effects as calorimeter cracks, non-linear energy response, or non-compensation. We therefore believe that a more accurate simulation should be employed to verify our results. However, we find our results to be in good agreement with previous work and believe that they form a reasonable basis from which to continue more detailed studies.

Acknowledgements

We would like to thank Jim Freeman and Cathy Newman-Holmes for their efforts in developing the QFL simulation. We would also like to thank Frank Paige and Sherban Protopopescu for the development and maintenance of the ISAJET Monte Carlo program. We would also like to acknowledge Lina Galtieri, Ian Hinchliffe and Marjorie Shapiro for their encouragement and advice during various stages of this work.

References

[1] K. Lane and J. Rohlf, SNOWMASS 84, p. 737.

[2] E. W. N. Glover and T. D. Gottschalk, SNOWMASS 86, p. 77.

[3] G. Herten, in Proceedings on Experiments, Detectors and Experimental Areas for the Supercollider, edited by R. Donaldson and M. G. D. Gilchreise (World-Scientific, Singapore, 1988), p. 103.

[4] K. J. Foley *et al.*, in Proceedings on Experiments, Detectors and Experimental Areas for the Supercollider, edited by R. Donaldson and M. G. D. Gilchreise (World-Scientific, Singapore, 1988), p. 701.

[5] F. Abe et al., Phys. Rev. Lett. **64**, 192 (1990).

[6] F. Abe et al., report in preparation.

[7] P. Langacker, Phys. Rev. Lett. **63**, 1920 (1989).

[8] F. Paige and S. Protopopescu, BNL Report No. BNL 38034, 1986 (unpublished).

[9] J. Freeman and C. Newman-Holmes, in Proceedings on Experiments, Detectors and Experimental Areas for the Supercollider, edited by R. Donaldson and M. G. D. Gilchreise (World-Scientific, Singapore, 1988), p. 673.

[10] J. Freeman and A. Beretvas, in SNOWMASS 86, p. 482.

[11] P. K. Sinervo, in Proceedings on the 1989 International Symposium on Lepton and Photon Interactions at High Energy, edited by M. Riordan (World-Scientific, Singapore, 1990), p. 328.

Table 1: The parameters used for the CLUSTR jet clustering.

Seed Tower E_T Threshold	2.0 GeV
Shoulder Tower E_T Threshold	0.2 GeV
Daughter Tower E_T Ratio	2.0
Cluster Merging Radius	0.7

Table 2: The effect of the electron selection.

Selection Requirement	Candidates Passing	% Passing
Initial Sample	30633	
$\|\eta\| < 3.0$	28005	92
$E_T >$ 20 GeV	21594	77
$h/em <$ 0.10	15491	72
EtBord$<$ 5.0 GeV	14501	94
EoverP$<$ 1.5	14422	99